PHOTONICS Research

Saturation efficiency for detecting 1550 nm photons with a 2 × 2 array of $Mo_{0.8}Si_{0.2}$ nanowires at 2.2 K

Feiyan Li,† Hang Han,† Qi Chen, Biao Zhang, Han Bao, Yue Dai, Rui Ge, Shuya Guo, Guanglong He, Yue Fei, Shuchao Yang, Xiaohan Wang, Hao Wang, Xiaoqing Jia, Qingyuan Zhao, Labao Zhang,* Lin Kang, and Peiheng Wu

School of Electronic Science and Engineering, Nanjing University, Nanjing 210023, China
**Corresponding author: Lzhang@nju.edu.cn*

Received 15 October 2020; revised 23 December 2020; accepted 29 December 2020; posted 19 January 2021 (Doc. ID 412697); published 1 March 2021

Amorphous materials are attractive candidates for fabricating the superconducting nanowire single-photon detectors (SNSPDs) due to their superior tolerance and scalability over crystalline niobium nitride. However, the reduced superconducting transition temperature degenerates both operating temperature and saturation efficiency. Herein, the SNSPD (6.5 nm thickness and 50 nm width) based on the amorphous $Mo_{0.8}Si_{0.2}$ film with a high optical absorption coefficient demonstrates close-to-unity intrinsic detection efficiency for 1550 nm photons from 75 mK to 2.2 K. Further, a high-performance array SNSPD with optimized 90 nm-width wires is also demonstrated. As-fabricated uniform 4-pixel SNSPD exhibits a saturation plateau for the photon counts at 2.2 K, which overcomes the limitation of operation at low temperature (< 1 K) for traditional amorphous SNSPDs. Coupled with superior intrinsic quantum efficiency, highly efficient photon counts, and low dark count ratio, this detector paves a way for achieving high efficiency and superior yield for large array systems.

https://doi.org/10.1364/PRJ.412697

1. INTRODUCTION

Since the fabrication of the first superconducting nanowire single-photon detector (SNSPD) by Gol'tsman *et al.* [1], SNSPDs have merged as the most prevalent single-photon detectors due to their high system detection efficiency (SDE) [2], remarkably low dark count rate (DCR) [3], low timing jitter [4], ultrashort recovery time [5], and high photon count rate (PCR) [6]. Moreover, SNSPDs as advanced technologies exhibit the high potential for various applications, such as quantum optics experiments [7], quantum key distribution (QKD) for quantum communication [8], fluorescent lifetime analysis for medical applications [9], space-to-ground optical communication [10], and integrated waveguide nanophotonic circuits [11].

High internal detection efficiency (IDE) and operating temperature have always been the permanent pursuit for SNSPD; however, it is difficult to optimize the two features simultaneously [12]. The restriction stems from the internal mechanism of single photon detection by the superconducting materials. At the same time, it remains challenging for widely used NbN materials to fabricate such devices due to the crystal defects and large energy gap [13]. For this, researchers have developed novel superconductors based on amorphous materials, which have been demonstrated as promising candidates for SNSPDs [14,15]. Compared to the polycrystalline materials, the amorphous films show clear advantages in terms of tolerance and scalability. The nanowires fabricated by using amorphous materials appear to suffer from fewer constrictions, along with the high yield on the Si wafers [16]. The disordered structure offers a high degree of homogeneity and significant compatibility in the optical cavity. Moreover, the films with low energy gap are noted to be sensitive to midinfrared wavelengths [17]. Therefore, SNSPDs based on amorphous films have the potential to emerge as the desirable choice to detect the wavelengths from near-infrared to midinfrared.

According to the Bardeen–Cooper–Schrieffer relation $2\Delta = 3.53k_BT_c$ [18], low energy gap results from low T_c, and vice versa. Based on this, the single-photon detectors fabricated from amorphous superconductors generally operate at low temperatures. For instance, the highest system detection efficiency (SDE) of 93% was achieved for the SNSPDs fabricated from amorphous WSi operated at 0.12 K at the National Institute of Standards and Technology (NIST) in 2013 [2], indicating that WSi-SNSPDs need to run below 1 K to achieve the optimal performance. In contrast, though the

superconducting energy gaps of the MoSi thin films are comparable to that of WSi, their T_c value is higher than 4 K [15]. Thus, the MoSi film becomes as a promising amorphous material for SNSPDs, which can be operated at $T > 2$ K temperature.

Recently, MoSi-SNSPDs have presented an excellent performance, with a detection efficiency higher than 95% at 0.7 K [19]. Besides, it has been demonstrated that a 1 μm-wide MoSi superconducting strip is capable of single-photon detection. A large active area (400 μm × 400 μm) of the microwire single-photon detector was fabricated, which exhibited the saturated photon counts at 0.3 K [16], suggesting that the MoSi film was competent for the fabrication of SNSPD with high efficiency and large area fabrication. As mentioned above, the single-photon detectors fabricated from amorphous superconductors generally operate at low temperatures to achieve the optimal performance, which hinders their development from the fundamental research phase to the practical application.

In this study, we fabricated SNSPDs with high-performance for both high T_c and high optical absorption coefficient of $Mo_{0.8}Si_{0.2}$ films.

2. EXPERIMENT

The fabrication of $Mo_{0.8}Si_{0.2}$ superconducting nanowires has been achieved by carrying out several processes, as illustrated in Fig. 1. Generally, high-resolution hydrogen silsesquioxane (HSQ) is prevalently used as a negative-tone resist to expose the ultranarrow linewidth nanowire. Nevertheless, the HSQ resist is not compatible with the $Mo_{0.8}Si_{0.2}$ nanowire patterning since the film suffers from a significant reduction in superconductivity performance after development in the standard HSQ developer tetramethylammonium hydroxide (TMAH). As reported, the positive-tone resist for achieving the nanowires with a sub-100 nm line width is difficult [11]. Thus, the high-quality nanowires with the narrow width for the MoSi films remain challenges. In this study, a well-known positive-tone resist PMMA 950K is utilized for exposure by electron beam lithography (EBL). By reducing the molecular weight of the PMMA resist and optimizing the EBL parameters and by incorporating reactive ion etching to overcome the various challenges, a sub-50 nm width nanowire with an active area of 20 μm × 20 μm is successfully fabricated.

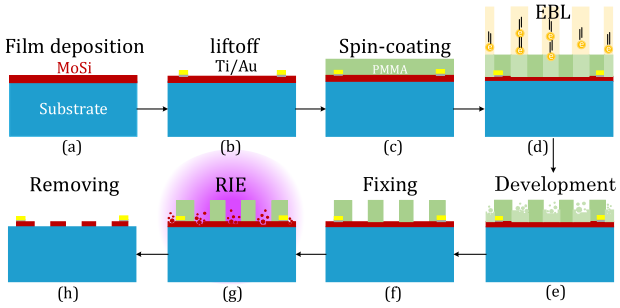

Fig. 1. (a) $Mo_{0.8}Si_{0.2}$ film deposition on a thermally oxidized silicon wafer. (b) Fabrication of electrode pads composed of Ti and Au by lithography and liftoff. (c) Spin-coating with electron-beam resist PMMA. (d) Meandering nanowire patterning by EBL. (e) Development in methyl isobutyl ketone (MIBK) diluted in isopropanol (IPA). (f) Fixing to obtain the mask pattern. (g) Pattern transfer to the film by RIE. (h) Removal of the residual resists using N-methyl pyrrolidone.

A. Growth of $Mo_{0.8}Si_{0.2}$ Thin Films

In this study, the 6.5 nm-thick $Mo_{0.8}Si_{0.2}$ film has been grown on the polished and thermally oxidized silicon wafer by employing the DC magnetron sputtering from an alloy target (4-in. diameter, 1 in. = 2.54 cm) with the stoichiometry of Mo:Si = 0.8:0.2. Before the film deposition, the sample is cleaned with Ar ion milling with the beam currents of 300 mA for 10 s and subsequently delivered to the chamber, followed by vacuum-pumping to 10^{-6} Pa. The sputtering process is performed at room temperature with 33 SCCM (standard cubic centimeter per minute) Ar gas, 45° throttle valve and 2 mTorr (1 Torr = 133.322 Pa) chamber pressure. Generally, the alloy target is presputtered for 5 min to clean the surface and stabilize the deposition conditions. The thickness of the film depends on the deposition rate (0.9 nm/s) and time.

Considering the poor antioxidant ability of the MoSi film, 4 nm-thick Nb_5N_6 grown on the film is carried out *in-situ* to prevent oxidation. The Nb_5N_6 film is deposited by an RF magnetron sputtering with RF power of 400 W in a 1:4 Ar and N_2 at 20 mTorr chamber pressure. Based on our previous experimental study, the chemical composition and crystalline structure of Nb_5N_6 have been analyzed by using an Auger electron energy spectrometer (AES) and X-ray diffractometer (XRD). The results indicate that the sample has a Nb/N ratio of 5:6, along with a hexagonal structure [20]. Further, the Nb_5N_6 film shows semiconducting electronic properties, in which the resistance rises as the temperature decreases, reaching >100,000 ohm at 4.2 K [21]. Thus, it is safe to suggest that the capping layer has no adverse impact on the superconducting film at low temperature. Simultaneously, the presence of the Nb_5N_6 capping layer also protects the film from degradation during the follow-up fabrication.

As shown in Fig. 2(a), the T_c is observed to be near 8 and 5.2 K for the 100 and 6.5 nm-thick films, respectively, and the

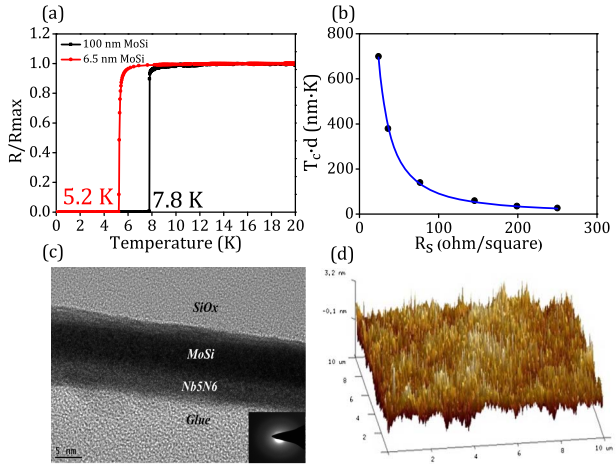

Fig. 2. (a) Comparison of the resistivity versus temperature curve of the 6.5 nm (red) and 100 nm (black) films. (b) $T_c d$ as a function of R_s obtained by fitting the universal scaling law proposed by Ivry *et al.* (c) TEM image of the film, the insert shows the diffraction ring pattern. (d) The surface roughness was measured using AFM. The roughness RMS is 0.5 nm.

superconducting transition width ΔT is 0.2 K. The universal scaling law ($T_c d = A \times R_s^{-B}$) proposed by Ivry *et al.* [22], is utilized to evaluate the film parameters. The fitting parameters A and B are 63752 ± 502 and 1.42 ± 0.03, respectively. The value of B must be greater than 1 for the amorphous films, which is in good agreement with the literature, confirming the amorphous nature of the film [15]. The morphological structure of the film has also been characterized by transmission electron microscopy (TEM). The presence of the disordered atomic structure in the film is confirmed from the absence of any sharp diffraction ring in the diffraction ring pattern. The surface roughness of the film has also been evaluated by atomic force microscopy (AFM), as illustrated in Fig. 2(d). The surface roughness is root-mean-square of 0.5 nm in the 10 μm × 10 μm images.

An overview of the prior work on the superconducting properties of the MoSi films has been presented in Table 1. The optimization of the film sputtering recipes to operate the devices at high temperatures has been presented. As expected, the T_c obtained in this study is higher than the other films, allowing the detectors to operate at $T > 2$ K.

The measurement of the optical constants of the film provides essential parameters for the simulation of the nanowire photon absorption and integrated optical structures. Here, the complex refractive index of the thin $Mo_{0.8}Si_{0.2}$ film has been measured by variable angle spectroscopic ellipsometry (VASE) with the wavelength ranging from 210 to 2500 nm, as shown in Fig. 3(a). The absorption efficiency of the device is calculated by the finite-difference time-domain (FDTD) method. The nanowires are sandwiched between a substrate and a SiO_2 dielectric superstrate, as depicted in the inset of Fig. 3(b). From the simulation results, the value of the absorption efficiency is observed to be 85%, which is higher than the literature studies [23,24], thus, suggesting that the high extinction coefficient can improve the detection efficiency of the SNSPDs. The difference in the absorption efficiency of the thin films is attributed to the fact that the optical properties of the MoSi films vary with the stoichiometry. Notably, the Mo-rich film has superior photon absorption performance as compared to the Mo-poor film, as confirmed by the comparison of the complex refractive index of the MoSi films with different stoichiometric ratios in Table 1. The extinction coefficient of the films is noted to increase with the Mo composition. Actually, the composition of the sputtered film may deviate from the composition of the alloy target. Though the composition of the film after deposition was not analyzed in this study, it is inferred that the stoichiometric ratio of the MoSi film is more than 0.83:0.17 rather than 0.8:0.2.

Table 1. Comparison of the Different Stoichiometric Ratios of the MoSi Films in Terms of Bulk T_c, Complex Refractive Index, and FDTD Simulation Results (1550 nm Wavelength)[a]

Film Stoichiometry	Bulk T_c	n	k	A
$Mo_{0.75}Si_{0.25}$ [28]	7.50	–	–	–
$Mo_{0.76}Si_{0.24}$ [14]	7.20	–	–	–
$Mo_{0.75}Si_{0.25}$ [23]	7.70	4.70	2.90	0.55
$Mo_{0.83}Si_{0.17}$ [24]	7.60	5.25	4.77	0.77
$Mo_{0.8}Si_{0.2}$ (this work)	7.80	5.57	5.85	0.85

[a] n = refractive index; k = extinction coefficient; A = absorption efficiency.

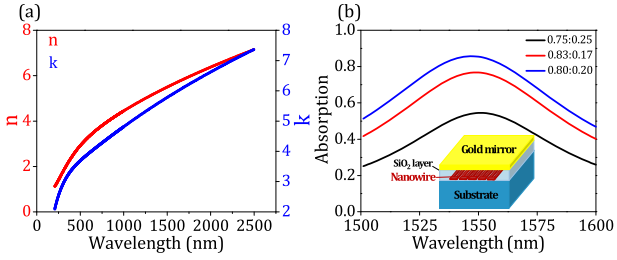

Fig. 3. (a) Complex refractive index of the $Mo_{0.8}Si_{0.2}$ film. (b) The simulation of the optical absorption of the nanowires with different stoichiometric ratios (1550 nm wavelength).

B. Fabrication of $Mo_{0.8}Si_{0.2}$ Superconducting Nanowires

The meandering nanowires are exposed with high-resolution positive-tone electron-beam resist PMMA by the EBL of the Raith EBPG 5200 at 100 keV electron beam with an area dose density of 800 μC/cm^2. After exposure, the chip is developed in MIBK: AIP with a ratio of 1:3 at 22°C for 90 s, followed by AIP treatment to fix the pattern for 60 s. The reactive ion etching (RIE) is used to transfer the nanowire pattern into the film. It is vital to optimize the RIE recipe for obtaining a high-quality nanowire pattern with smooth and vertical sidewalls and uniform lines [25]. The unprotected film is removed by RIE in CF_4. The reaction during the RIE process is described as follows [26,27]:

$$CF_4 \rightarrow CF_3 + F, \quad (1)$$

$$Nb_5N_6 + 15F \rightarrow 5NbF_3\uparrow + 3N_2\uparrow, \quad (2)$$

$$MoSi + 10F \rightarrow MoF_6\uparrow + SiF_4\uparrow, \quad (3)$$

where, F represents the fluorine radicals, which are ionized from the CF_4 gas by glow discharge in the etching chamber. The Nb_5N_6 capping layer is on top of the MoSi film; thus, there is a different etching effect based on the composition of the two layers. Here, the fluorine radicals react with the capping layer Nb_5N_6 and $Mo_{0.8}Si_{0.2}$ film in order, resulting in the production of the volatile gaseous material. Two steps are employed for the etching time evaluation. First, the film is etched to estimate the optimal etching duration, termed as T_f. Once the film is completely etched, the resistance reaches the G ohm level, indicating the bare substrate on the outside. At this phase, the T_f value is 100 s. Subsequently, the etching time for the nanowires is optimized based on T_f, by comparing the difference between the theoretical and experimental resistance values after etching and characterizing the size and line morphology of the nanowires with SEM, as portrayed in Fig. 4. The experimental resistance value of the nanowire is noted to be comparable to the theoretical value for the etching duration of 110 s.

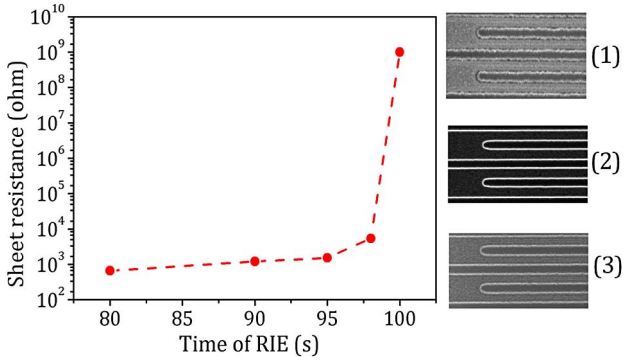

Fig. 4. Estimation of the total etching time for the $Mo_{0.8}Si_{0.2}$ film, and the optimization of the nanowires etching, representing: (1) under-etching, (2) optimum etching, (3) over-etching.

3. RESULTS AND DISCUSSION

Figure 5 shows the 6.5 nm-thick film with 50 nm wide nanowires; the developed nanowire-shape has been depicted in detail in the magnified images. Considering the positive-tone resist with the properties of low-accuracy and high-sensitivity for lithography, and poor resistance to chemical etching, the devices are vulnerable owing to the constrictions attributed to the proximity effect. Thus, it is difficult for the PMMA resist to obtain the nanowires with <80 nm width in the large active area. Here, by using a low concentration of the PMMA resist as well as pattern compensation for relieving the proximity effect, the linewidth of the nanowires is noted to deviate below 5 nm.

The electrical and optical properties of the SNSPDs have been investigated using two conditions: dilution refrigerator with water-cooled closed-cycle augmented by a ^{4}He sorption pump unit and Gifford–McMahon cryocooler operating at 2.2 K. Figure 6(a) shows the current-voltage curves of the superconducting nanowires with a width of 50 nm, an active area of 20 μm × 20 μm and the filling factor of 0.25 under different operating temperatures ranging from 75 mK to 2.2 K. The switching current I_{SW}, i.e., the bias current at which the

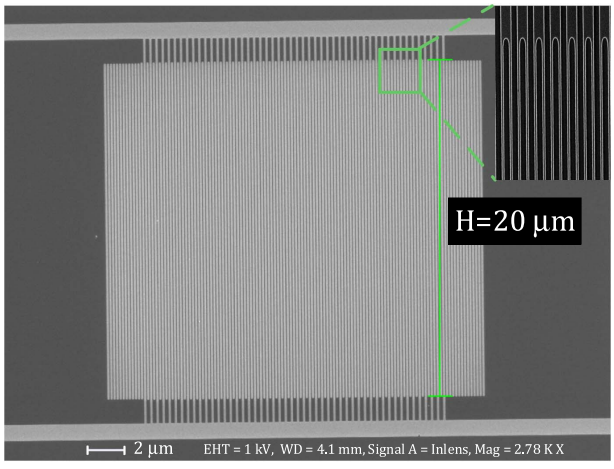

Fig. 5. SEM images of the $Mo_{0.8}Si_{0.2}$ nanowires fabricated using the PMMA resist, the nanowires with a line width of 50 ± 2 nm, a period of 200 nm, and an active area of 20 μm × 20 μm.

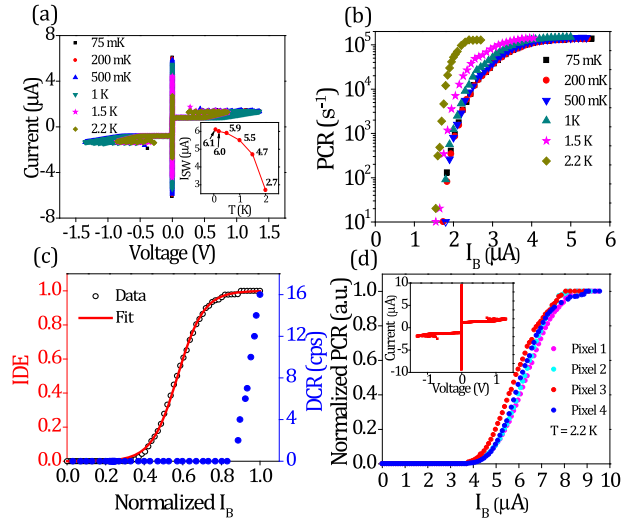

Fig. 6. (a) *I-V* curves of single pixel SNSPD with 50 nm-width nanowires at different operating temperatures, ranging from 75 mK to 2.2 K. The inset figure presents I_{SW} as a function of temperature. (b) The photon counts as functions of the bias current at different operating temperatures for the single pixel SNSPD. (c) Internal detection efficiency (IDE) and dark count rate (DCR) as functions of the normalized bias current for 50 nm-width nanowires. (d) Normalized photon counts as a function of the bias current for the 4-pixel based $Mo_{0.8}Si_{0.2}$ – SNSPD at 2.2 K, the inset in the lower right corner depicts the *I-V* curve of one of the pixels.

device switches from the superconducting to the normal state, gradually decreases with enhancing the temperature. The I_{SW} values are noted to be 6.1 and 2.7 μA at 75 mK and 2.2 K, respectively.

The photon counting measurement is carried out with continuous tunable laser at 1550 nm, and the input photon flux is attenuated by the two serial variable attenuators to a level of 10^6 photons/s, calibrated with a highly precise light power meter (Thorlabs-PM100D). The SNSPDs are illuminated by using a single module fiber coupled with the input light into detector. Figure 6(b) exhibits the photon count rate (PCR) as a function of the bias current (I_B) at different operating temperatures. Notably, the device has a saturated count rate ranging from 75 mK to 2.2 K. The saturation of the PCR versus I_B curves indicates that the detector quantum efficiency is also saturated [17]. The observed behavior suggests that the device reaches its 100% internal detection efficiency [28]. Figure 6(c) demonstrates the internal detection efficiency of the 50 nm-width SNSPD, which reveals a sigmoidal dependence on the normalized bias current, with saturation at $0.8I_{SW}$, where the DCR value is below 1 cps. To extract the saturation level of the detector, the bias dependence of IDE is fitted with an empirical sigmoid function [29]. The red solid line in Fig. 6(c) represents the fitting curve, where the maximum IDE reaches 100%.

Notably, as a proof of the array detector, a 4-pixel array device with 90 nm-width, a period of 200 nm, and an active area of 40 μm × 40 μm has explicitly been fabricated. Figure 6(d) shows the normalized photon counts as a function of the bias

current for the 4-pixel device operating at 2.2 K (inset depicting the *I-V* curve of one of the pixels). The I_{SW} is noted to be 9.5 μA with the hysteresis current of 1 μA, which is higher than the waveguide-integrated nanowire of 3.3 μA reported by Häußler [11], resulting in a higher signal-to-noise ratio. As demonstrated in the previous literature studies [28], the $Mo_{0.75}Si_{0.25}$ – SNSPD with a nanowire width of 110 nm and an active area of 16 μm × 16 μm exhibited saturated internal efficiency at 2.3 K. The nanowire geometric defects and constrictions are proportional to the length, and the length of the nanowires is also proportional to the active area for the same size (width and pitch) of the nanowires. Therefore, it is extremely challenging to achieve the saturated efficiency at high temperatures for large active areas. In this study, the 4-pixel array device with 90 nm-width nanowires and an active area of 40 μm × 40 μm has explicitly been fabricated, exhibiting the saturated intrinsic detection efficiency at a temperature of 2.2 K.

The *I-V* curves of the 4 pixels are noted to be similar for the switching current ranging from 9.0 μA to 9.5 μA. We have calculated the depairing current of SNSPD according to the equations presented by Korneeva *et al.* [30]. Herein, The I_{dep} (2.2 K) is 14.5 μA; we found the ratio of I_{SW}/I_{dep} to be in the range of 0.62–0.65. This ratio supports the fact of the little constrictions during array SNSPD fabrication. Specifically, it is seen that the photon count of each pixel exhibits a saturation plateau, indicating the close-to-unity internal detection efficiency. The photon count of each pixel exhibits the maximum count rate of 10^5 s^{-1} with $<10^3$ cps dark counts at 2.2 K. Recently, the superconducting microwire was used for single photon detection with the aim of achieving saturated internal detection efficiency over a large area. The results exhibited the saturated internal detection efficiency for 1550 nm wavelengths at 0.3 K [16]. Such detectors rely on a very low temperature (mK) to achieve their excellent performance, thus, limiting the application for single photon detection. Considering that the cryogenic requirements are less complicated and less costly at 2.2 K than at <1 K, it is beneficial to have devices with optimal saturation efficiency at high temperatures, which debases the demand for the cryogenic systems and simplifies the integration of device measurement.

4. CONCLUSION

In conclusion, this work demonstrates the amorphous $Mo_{0.8}Si_{0.2}$ film exhibiting a high optical absorption coefficient in the visible to midinfrared range. The SNSPD fabricated from the $Mo_{0.8}Si_{0.2}$ film with 6.5 nm-thickness and 50 nm-width demonstrates the saturated intrinsic detection efficiency with sub 1 Hz dark count rate at a temperature of 0.2 K. Particularly, a uniform 4-pixel SNSPD has been successfully developed, exhibiting a saturation plateau for the photon counts at a temperature of 2.2 K. As a whole, the SNSPD based on $Mo_{0.8}Si_{0.2}$ films exhibits excellent advantages in operation temperature, spectral sensitivity, and internal detection efficiency.

Funding. National Key Research and Development Program of China (2017YFA0304002); National Natural Science Foundation of China (12033002, 62071218, 61521001, 62071214, 61801206, 11227904); Key-Area Research and Development Program of Guangdong Province (2020B0303020001); Fundamental Research Funds for the Central Universities; Priority Academic Program Development of Jiangsu Higher Education Institutions; Recruitment Program for Young Professionals; Qing Lan Project; Jiangsu Provincial Key Laboratory of Advanced Manipulating Technique of Electromagnetic Waves.

Disclosures. The authors declare no conflicts of interest.

†These authors contributed equally to this paper.

REFERENCES

1. G. N. Gol'tsman, O. Okunev, G. Chulkova, A. Lipatov, A. Semenov, K. Smirnov, B. Voronov, A. Dzardanov, C. Williams, and R. Sobolewski, "Picosecond superconducting single-photon optical detector," Appl. Phys. Lett. **79**, 705–707 (2001).
2. F. Marsili, V. B. Verma, J. A. Stern, S. Harrington, A. E. Lita, T. Gerrits, I. Vayshenker, B. Baek, M. D. Shaw, R. P. Mirin, and S. W. Nam, "Detecting single infrared photons with 93% system efficiency," Nat. Photonics **7**, 210–214 (2013).
3. H. Shibata, K. Shimizu, H. Takesue, and Y. Tokura, "Superconducting nanowire single-photon detector with ultralow dark count rate using cold optical filters," Appl. Phys. Express **6**, 072801 (2013).
4. B. Korzh, Q. Y. Zhao, J. P. Allmaras, S. Frasca, T. M. Autry, E. A. Bersin, A. D. Beyer, R. M. Briggs, B. Bumble, M. Colangelo, G. M. Crouch, A. E. Dane, T. Gerrits, A. E. Lita, F. Marsili, G. Moody, C. Peña, E. Ramirez, J. D. Rezac, N. Sinclair, M. J. Stevens, A. E. Velasco, V. B. Verma, E. E. Wollman, S. Xie, D. Zhu, P. D. Hale, M. Spiropulu, K. L. Silverman, R. P. Mirin, S. W. Nam, A. G. Kozorezov, M. D. Shaw, and K. K. Berggren, "Demonstration of sub-3 ps temporal resolution with a superconducting nanowire single-photon detector," Nat. Photonics **14**, 250–255 (2020).
5. F. Marsili, F. Najafi, E. Dauler, R. J. Molnar, and K. K. Berggren, "Afterpulsing and instability in superconducting nanowire avalanche photodetectors," Appl. Phys. Lett. **100**, 112601 (2012).
6. T. Polakovic, W. Armstrong, V. Yefremenko, J. Pearson, K. Hafidi, G. Karapetrov, Z. E. Meziania, and V. Novosad, "Superconducting nanowires as high-rate photon detectors in strong magnetic fields," Nucl. Instrum. Methods Phys. Res. A **959**, 163543 (2020).
7. P. V. Klimov, A. L. Falk, D. J. Christle, V. V. Dobrovitski, and D. D. Awschalom, "Quantum entanglement at ambient conditions in a macroscopic solid-state spin ensemble," Sci. Adv. **1**, e1501015 (2015).
8. M. Pereira, G. Kato, A. Mizutani, M. Curty, and K. Tamaki, "Quantum key distribution with correlated sources," Sci. Adv. **6**, eaaz4487 (2020).
9. J. Yamamoto, M. Oura, T. Yamashita, S. Miki, T. Jin, T. Haraguchi, Y. Hiraoka, H. Terai, and M. Kinjo, "Rotational diffusion measurements using polarization-dependent fluorescence correlation spectroscopy based on superconducting nanowire single-photon detector," Opt. Express **23**, 32633–32642 (2015).
10. N. Horiuchi, "Long-distance teleportation," Nat. Photonics **9**, 707 (2015).
11. M. Häußler, M. Y. Mikhailov, M. A. Wolff, and C. Schuck, "Amorphous superconducting nanowire single-photon detectors integrated with nanophotonic waveguides," Appl. Phys. Lett. **5**, 076106 (2020).
12. I. Holzman and Y. Ivry, "Superconducting nanowires for single-photon detection: progress, challenges, and opportunities," Adv. Quantum Technol. **2**, 1800058 (2019).
13. S. Miki, T. Yamashita, H. Terai, and Z. Wang, "High performance fiber-coupled NbTiN superconducting nanowire single photon detectors with Gifford-McMahon cryocooler," Opt. Express **21**, 10208–10214 (2013).

14. A. E. Lita, V. B. Verma, R. D. Horansky, J. M. Shainline, R. P. Mirin, and S. Nam, "Materials development for high efficiency superconducting nanowire single-photon detectors," Mater. Res. Soc. Symp. Proc. **1807**, 1–6 (2015).
15. A. Banerjee, M. Nord, Z. H. Barber, I. MacLaren, A. Doye, K. Erotokritou, D. Bosworth, and L. J. Baker, "Characterisation of amorphous molybdenum silicide (MoSi) superconducting thin films and nanowires," Supercond. Sci. Technol. **30**, 084010 (2017).
16. I. Charaev, Y. Morimoto, A. Dane, A. Agarwal, M. Colangelo, and K. K. Berggren, "Large-area microwire MoSi single-photon detectors at 1550 nm wavelength," Appl. Phys. Lett. **116**, 242603 (2020).
17. V. B. Verma, A. E. Lita, B. A. Korzh, E. Wollman, M. Shaw, R. P. Mirin, and S.-W. Nam, "Towards single-photon spectroscopy in the mid-infrared using superconducting nanowire single-photon detectors," Proc. SPIE **10978**, 109780N (2019).
18. M. Tinkham and J. C. Wheatley, "Introduction to superconductivity," Phys. Today **29**, 57 (1976).
19. D. V. Reddy, R. R. Nerem, A. E. Lita, S. W. Nam, R. P. Mirin, and V. B. Verma, "Exceeding 95% system efficiency within the telecom C-band in superconducting nanowire single photon detectors," in *CLEO: QELS Fundamental Science* (2019), paper FF1A.3.
20. X. H. Lu, N. He, L. Kang, J. Chen, B. B. Jin, and P. H. Wu, "Nb_5N_6 thin film on silicon and silicon oxide: a good material for terahertz detection," Chin. Sci. Bull. **54**, 3344–3346 (2009).
21. X. Q. Jia, L. Kang, M. Gu, X. Z. Yang, C. Chen, X. C. Tu, B. B. Jin, W. W. Xu, J. Chen, and P. H. Wu, "Fabrication of a strain-induced high performance NbN ultrathin film by a Nb_5N_6 buffer layer on Si substrate," Supercond. Sci. Technol. **27**, 035010 (2014).
22. Y. Ivry, C. Kim, A. E. Dane, D. De Fazio, and A. Mccaughan, "Universal scaling of the critical temperature for thin films near the superconducting-to-insulating transition," Phys. Rev. B **90**, 214515 (2014).
23. V. B. Verma, B. Korzh, F. Bussières, R. D. Horansky, S. D. Dyer, A. E. Lita, I. Vayshenker, F. Marsili, M. D. Shaw, H. Zbinden, R. P. Mirin, and S. W. Nam, "High-efficiency superconducting nanowire single-photon detectors fabricated from MoSi thin-films," Opt. Express **23**, 33792–33801 (2015).
24. J. Li, R. A. Kirkwood, L. J. Baker, D. Bosworth, K. Erotokritou, A. Banerjee, R. M. Heath, C. M. Natarajan, Z. H. Barber, M. Sorel, and R. H. Hadfield, "Nano-optical single-photon response mapping of waveguide integrated molybdenum silicide (MoSi) superconducting nanowires," Opt. Express **24**, 13931–13938 (2016).
25. I. Charaev, T. Silbernagel, B. Bachowsky, A. Kuzmin, S. Doerner, K. Ilin, A. Semenov, D. Roditchev, D. Y. Vodolazov, and M. Siegel, "Enhancement of superconductivity in NbN nanowires by negative electron-beam lithography with positive resist," J. Appl. Phys. **122**, 083901 (2017).
26. T. T. Foxe, B. D. Hunt, C. Rogers, A. W. Kleinsasser, and R. A. Buhrman, "Reactive ion etching of niobium," J. Vac. Sci. Technol. **19**, 1394–1397 (1981).
27. T. P. Chow and A. J. Steckl, "Plasma etching characteristics of sputtered $MoSi_2$ films," Appl. Phys. Lett. **37**, 466–468 (1980).
28. Y. P. Korneeva, M. Y. Mikhailov, Y. P. Pershin, N. N. Manova, A. V. Divochiy, Y. B. Vakhtomin, A. A. Korneev, K. V. Smirnov, A. G. Sivakov, A. Y. Devizenko, and G. N. Goltsman, "Superconducting single-photon detector made of MoSi film," Supercond. Sci. Technol. **27**, 095012 (2014).
29. T. Yamashita, S. Miki, H. Terai, and Z. Wang, "Low-filling-factor superconducting single photon detector with high system detection efficiency," Opt. Express **21**, 27177–27184 (2013).
30. Y. P. Korneeva, D. Y. Vodolazov, A. V. Semenov, I. N. Florya, N. Simonov, E. Baeva, A. A. Korneev, G. N. Goltsman, and T. M. Klapwijk, "Optical single-photon detection in micrometer-scale NbN bridges," Phys. Rev. Appl. **9**, 064037 (2018).